Journal of Power Sources 450 (2020) 227659

Contents lists available at ScienceDirect

Journal of Power Sources

journal homepage: www.elsevier.com/locate/jpowsour

Hollow carbon spheres codoped with nitrogen and iron as effective electrocatalysts for oxygen reduction reaction

Yumeng Ma [a,1], Shasha Luo [a,1], Minghua Tian [a], Jia En Lu [b], Yi Peng [b], Cooper Desmond [b], Qiming Liu [b], Qiaoxia Li [a,b,c,*], Yulin Min [a], Qunjie Xu [a,c], Shaowei Chen [b,**]

[a] Shanghai Key Laboratory of Materials Protection and Advanced Materials in Electric Power, College of Environmental and Chemical Engineering, Shanghai University of Electric Power, 2588 Changyang Road, Yangpu District, Shanghai, 200090, China
[b] Department of Chemistry and Biochemistry, University of California, 1156 High Street, Santa Cruz, CA, 95064, USA
[c] Shanghai Institute of Pollution Control and Ecological Security, Shanghai, 200090, China

HIGHLIGHTS

- Polystyrene nanoparticles as solid templates.
- Pyrolytic preparation of N,Fe-codoped hollow porous carbon spheres (FeNC).
- FeNC composites exhibit a large surface area and abundant FeN_x sites.
- FeNC-950 shows the best ORR activity, stability and methanol tolerance.

GRAPHICAL ABSTRACT

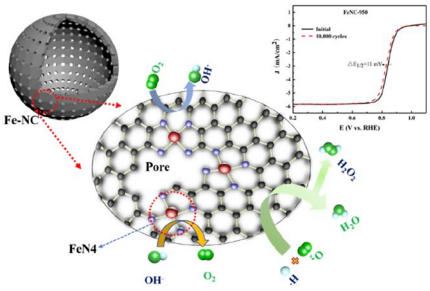

ARTICLE INFO

Keywords:
Metal-organic framework
Doped carbon
Hollow sphere
Oxygen reduction reaction
Alkaline fuel cell

ABSTRACT

Design and engineering of low-cost, effective catalysts for oxygen reduction reaction (ORR) plays a critical role in the development of fuel cells and metal-air batteries. Herein, we describe a facile template-assisted strategy for the fabrication of hollow porous carbon spheres codoped with nitrogen and iron species (FeNC) for ORR electrocatalysis. The samples are synthesized via one-step pyrolysis of a core-shell precursor, which is prepared by in-situ growth of a Fe-doped zeolite imidazolate framework (ZIF) shell onto the surface of polystyrene nanoparticles. The obtained FeNC composites exhibit a unique hollow structure with a large surface area, hierarchical porosity, and abundant FeN_x sites. Notably, the sample prepared at 950 °C (FeNC-950) exhibits the best ORR activity among the series in alkaline media (with an onset and half-wave potential at +0.94 and + 0.84 V vs. RHE, respectively), a performance on par with that of Pt/C and leading relevant catalysts reported in recent literature, where ORR proceeds mostly via the efficient four-electron reduction pathway. The FeNC-950 catalyst also displays superior stability and tolerance to methanol, as compared to commercial Pt/C. The results suggest that high-performance ORR catalysts can be derived by deliberate structural engineering of the metal-organic framework precursors.

* Corresponding author. Shanghai Key Laboratory of Materials Protection and Advanced Materials in Electric Power, College of Environmental and Chemical Engineering, Shanghai University of Electric Power, 2588 Changyang Road, Yangpu District, Shanghai, 200090, China.
** Corresponding author.
E-mail addresses: liqiaoxia@shiep.edu.cn (Q. Li), shaowei@ucsc.edu (S. Chen).
[1] These authors contributed equally to the work.

https://doi.org/10.1016/j.jpowsour.2019.227659
Received 11 November 2019; Received in revised form 19 December 2019; Accepted 23 December 2019

1. Introduction

Oxygen reduction reaction (ORR) is a cathode reaction of fuel cells and metal-air batteries that plays a critical role in determining the device performance [1–4]. At the present, platinum and its alloys are considered to be the best ORR electrocatalysts; however, they are prone to methanol and carbon monoxide poisoning, and their scarcity and high costs have greatly hindered large-scale commercialization of the technologies [5–10]. In recent years, catalysts composed of porous carbon doped with nitrogen and non-precious transition metals (MNC) have attracted widespread attention due to their high electrocatalytic performance, good corrosion resistance, and low costs [11–16], mostly due to the formation of MN_x coordination moieties [17–20].

In general, high electrocatalytic activity of MNC composites can be achieved with uniform nitrogen doping and transition metal distribution, high specific surface area, and high electrical conductivity [21–23]. Towards this end, hollow carbon nanostructures represent a unique structural scaffold [24–30], which can be constructed by exploiting precursors based on metal-organic frameworks (MOFs) [23, 31–34]. For instance, ZIF-8 features a zeolitic imidazole ester skeleton that has been shown to lead to the production of porous carbon with a high surface area and nitrogen doping by controlled pyrolysis. However, the ORR activity in general remains subpar as compared to that of commercial Pt/C [33–35]. The performance can be further improved by introducing a transition metal, such as Fe, into the ZIF precursor, which upon pyrolysis produces Fe–N active sites [36].

Herein, we describe a facile bottom-up strategy to fabricate highly porous and hollow Fe,N-codoped carbon spheres by one-step pyrolysis of a core-shell composite precursor consisting of carboxylate-terminated polystyrene nanoparticles as the core and bimetallic ZnFe-ZIF as the shell. In the pyrolysis process, the incorporation of Zn species in ZnFe-ZIF spatially separated the Fe species and impeded the aggregation of Fe nanoparticles, and concurrently afforded high porosity due to thermal evaporation. In addition, the polystyrene core was decomposed to afford the hollow structure, and the bimetallic ZIF shell was converted to hollow porous N-doped carbon spheres. Concurrently, pores and channels of different length scales were constructed together with doping, and Fe species from ZnFe-ZIF were dispersed into the carbon matrix forming FeN_x moieties. These unique features were found to facilitate the electron transfer and mass transfer involved in the ORR process, leading to effective ORR electrocatalysis. In fact, the obtained FeNC nanocomposites were found to display a high surface area, good degree of graphitization, abundant active sites, and thus remarkable ORR activity in alkaline media. Of these, the sample prepared at 950 °C exhibited the best electrocatalytic performance, which was on par with leading results of relevant Fe-based catalysts and commercial Pt/C (20 wt%).

2. Experimental section

2.1. Preparation of materials

Preparation of carboxylate-terminated polystyrene nanospheres. Polystyrene nanospheres were prepared by adopting a previously reported method [36]. In a typical synthesis, a mixture containing 21 mL of styrene, 1.1 mL of methyl methacrylate, 0.92 mL of acrylic acid and 0.49 g of NH_4HCO_3 was added to 100 mL of deionized water under mechanical stirring. When the temperature was raised to 70 °C, 0.53 g of ammonium persulfate was added to the solution, which was then heated at 80 °C for 12 h. A white precipitate was produced, which was separated by centrifugation, rinsed with deionized water several times, and finally freeze-dried for future use.

Preparation of polystyrene@ZIF core@shell nanospheres. In a typical procedure, $Zn(NO_3)_2{\cdot}6H_2O$ (591.28 mg) and $Fe(NO_3)_3{\cdot}9H_2O$ (20.2 mg) were dissolved in 100 mL of methanol. Separately, the polystyrene nanospheres obtained above (300 mg) and 2-methylimidazole (694.98 mg) were added into 100 mL of methanol under sonication for 30 min. These two solutions were mixed and heated at 60 °C for 24 h, producing a precipitant which was collected by centrifugation, rinsed with ethanol and dried at 70 °C in a vacuum oven for further use. The resultant product was denoted as PS@ZnFe-ZIF.

Preparation of FeNC nanocomposites. In a typical synthesis, the PS@ZnFe-ZIF precursor produced above was placed in a tube furnace and heated at a controlled temperature varied from 750 to 1050 °C for 2 h at a heating rate of 2 °C min^{-1} from room temperature under a nitrogen gas flow, resulting in the formation of hollow, porous carbon spheres codoped with N and Fe. The samples were denoted as FeNC-T, with T being the pyrolysis temperature (i.e., 750, 850, 950, or 1050 °C).

2.2. Structural characterization

The sample morphology was studied by using scanning electron microscopy (SEM) on a Hitachi SU 70 microscope at the working voltage of 5 kV. The microstructures and chemical composition of the products were characterized by using transmission electron microscopy (TEM, JEOL JEM-2100F) and energy dispersive X-ray spectroscopy (EDS, OXFORD, X-Max). Crystal structures were examined by X-ray diffraction (XRD, Bruker, D8 ADVANCE) measurements with Cu Kα radiation (λ = 0.15418 nm). X-ray photoelectron spectroscopy (XPS) studies were performed using a Kratos AXIS Ultra DLD XPS system equipped with a hemispherical energy analyzer and a monochromatic Al K_α source operated at 15 keV and 150 W. Nitrogen adsorption/desorption isotherms were recorded at 77 K on an ASAP 2460 instrument. Raman spectra were acquired on a LabRAM HR Evolution Raman spectrometer at 633 nm excitation.

2.3. Electrochemistry

Voltammetric measurements were carried out on a CHI 760E electrochemical workstation (CHENHUA Instrument, China) in a conventional three-electrode cell. A glassy carbon rotating disk electrode (GC-RDE, 5 mm in diameter) was used as the working electrode. A graphite rod was employed as the counter electrode and a Ag/AgCl electrode as the reference electrode. The Ag/AgCl reference electrode was calibrated against a reversible hydrogen electrode (RHE) and all potentials in the present study were referenced to this RHE. The working electrode was prepared as follows: 6 mg of the FeNC catalysts prepared above, 500 μL of ethanol, 500 μL of ultrapure water, and 50 μL of a Nafion solution (5 wt%) were mixed under sonication for 1 h to obtain a catalyst ink. Then, 20 μL of the ink was dropcast onto the freshly polished glassy carbon electrode and dried at room temperature. Prior to data acquisition, the electrolyte solution was purged with ultrahigh-purity N_2 or O_2 for 30 min. Cyclic voltammograms (CV) were acquired at the scan rate of 50 mV s^{-1}. Linear-sweep voltammetry (LSV) measurements were carried out at the scan rate of 5 mV s^{-1} with the rotation rate varied from 450 to 2500 rpm. All electrochemical experiments were performed at room temperature (25 ± 1 °C).

The number of electron transfer (n) and peroxide yield (H_2O_2%) were calculated using the following equations, $n = 4\frac{I_d}{I_d + \frac{I_r}{\eta_N}}$ and $H_2O_2(\%) = 200\%\frac{\frac{I_r}{N}}{I_d + I_r}$, where I_d and I_r represent the disk and ring current, respectively, and N is the ring collection efficiency (0.37) [37].

3. Results and discussion

3.1. Morphology characterization

The morphology and internal structure of the PS@ZnFe-ZIF precursor and FeNC-950 nanocomposites were first examined and compared by SEM and TEM measurements. From the SEM image in Fig. 1a, one can see that ZnFe-ZIF was adsorbed on the outer surface of the polystyrene nanoparticle, producing a rough surface and a quasi-core-shell structure.

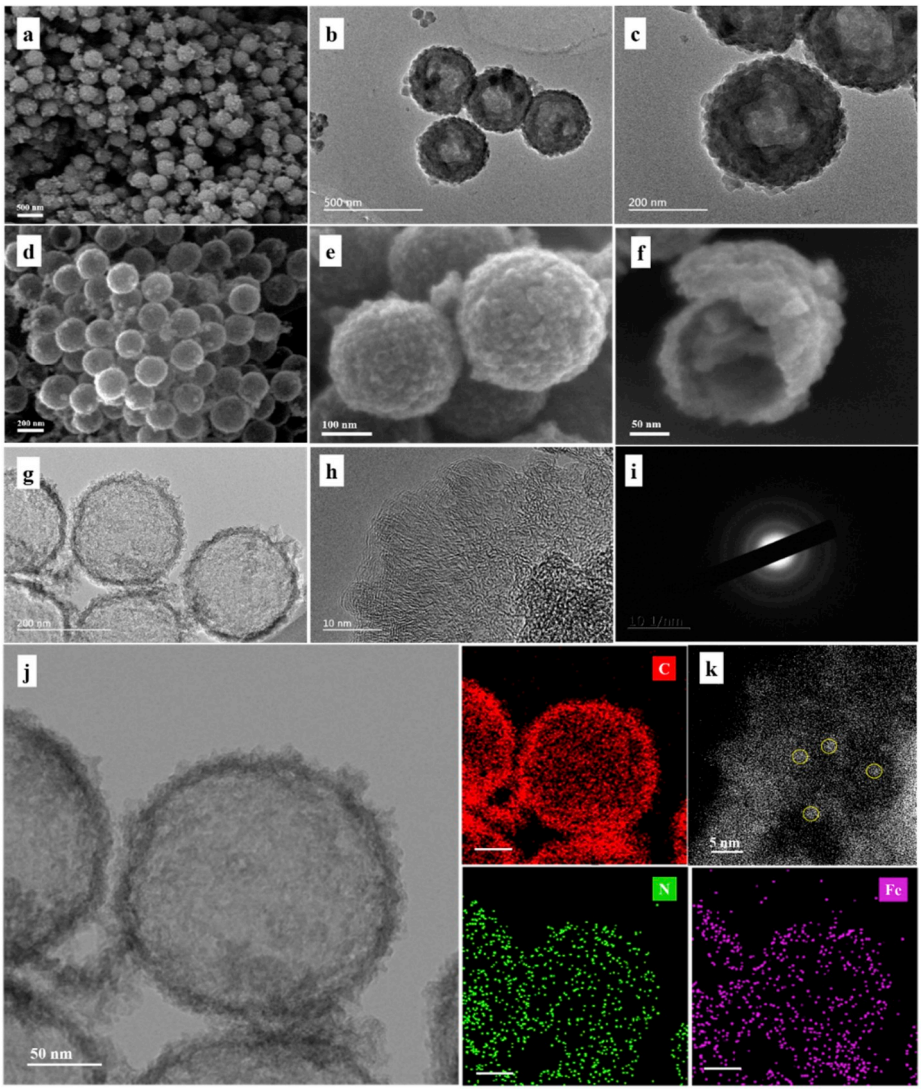

Fig. 1. (a) SEM and (b.c) TEM images of PS@ZnFe-ZIF precursor. (d–f) SEM, (g,h) TEM, (i) selected-area electron diffraction (SAED) pattern, (j) STEM and (k) HAADF-STEM images, and EDS elemental maps of the FeNC-950 sample.

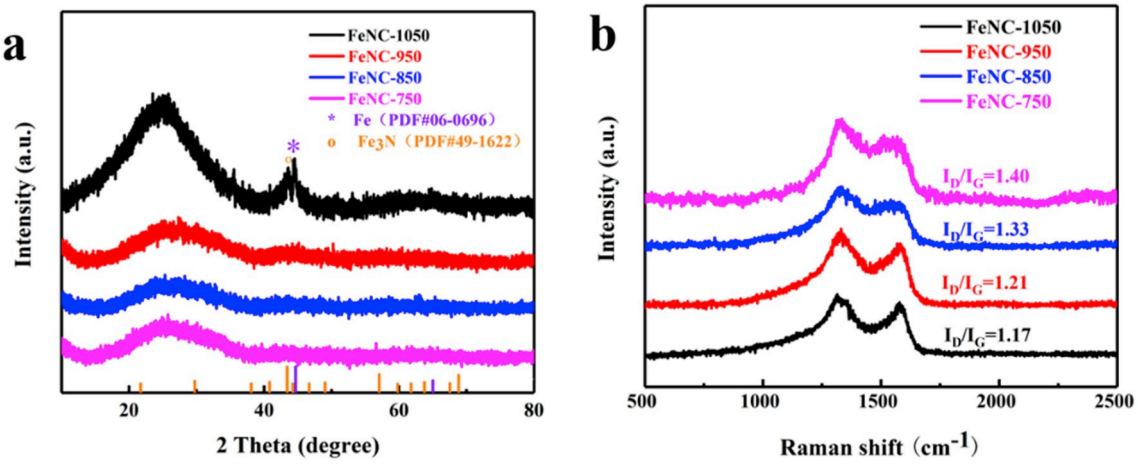

Fig. 2. (a) XRD patterns and (b) Raman spectra of FeNC-750, FeNC-850, FeNC-950, and FeNC-1050.

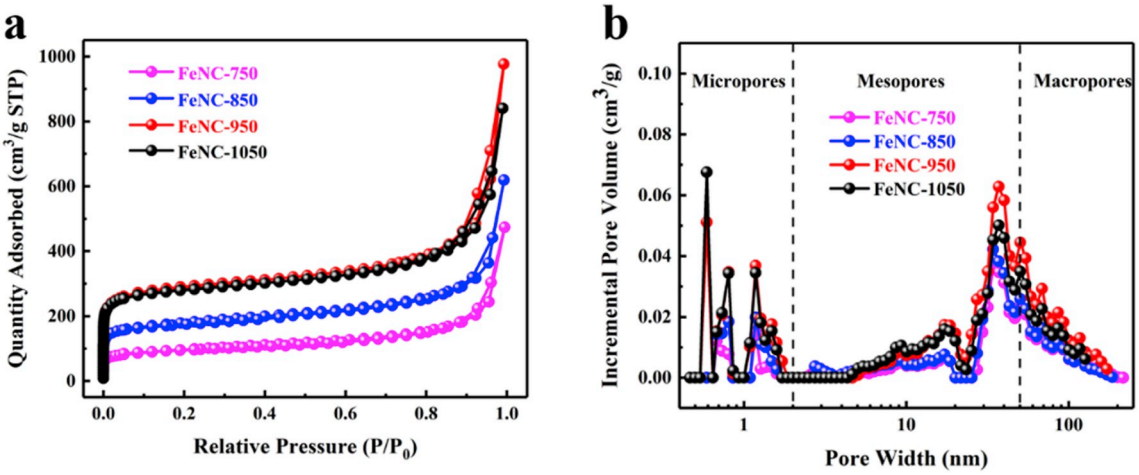

Fig. 3. (a) Nitrogen adsorption-desorption isotherms and (b) pore distributions of FeNC-750, FeNC-850 FeNC-950 and FeNC-1050.

Table 1
BET surface area, pore volume and pore size of FeNC-750, FeNC-850, FeNC-950, and FeNC1050.

Sample	BET Surface Area (m^2 g^{-1})	Pore Volume (cm^3 g^{-1})	Pore Size (nm)
FeNC-750	320.4	0.73	19.7
FeNC-850	577.7	0.96	15.2
FeNC-950	916.2	1.51	17.2
FeNC-1050	863.0	1.30	15.0

This in essence took advantage of the large number of –COOH functional groups on the polystyrene surface (Fig. S1) to anchor metal ions and nanocrystals, forming a lychee-like structure of the PS@ZnFe- ZIF precursor. From the TEM images (Fig. 1b and c), PS@ZnFe-ZIF can be seen to exhibit a rather uniform size (ca. 350 nm in diameter) and good dispersion. After pyrolysis, the resulting samples retained a consistent morphology, as manifested in SEM measurements of FeNC-950 (Fig. 1d–f), but featured a hollow structure, as evidenced in TEM study (Fig. 1g), with an outer diameter of about 240 nm and shell thickness of ca. 10 nm. This size was smaller than that of the polystyrene nanoparticle templates, likely because of the inward collapse of the adsorbed ZnFe-ZIF structure during the thermal removal of the polystyrene nanoparticles. Fig. 1h shows a high-resolution TEM image of the FeNC-950 sample, where short-range crystallinity can be seen [38], consistent with the corresponding selected area electron diffraction (SAED) patterns in Fig. 1i [39]. From the HAADF-STEM image (Fig. 1j and k), the Fe, C and N elements can be readily identified in FeNC-950, indicating the successful preparation of Fe,N-codoped carbon, whereas no Zn signal was detected, confirming the effective evaporation of the Zn species. Notably, no particulate materials were observed, implying that the Fe species were atomically dispersed within the carbon skeletons. In fact, the bright spots (white circles) in Fig. 1k can be ascribed to atomic Fe species in FeNC-950.

The structure of the FeNC composites was further characterized by XRD measurements. As depicted in Fig. 2a, all samples showed a broad diffraction peak at $2\theta = 26^\circ$, which can be assigned to the typical (002) diffraction of graphitic carbon [40], confirming the successful carbonization of the MOF precursors. In addition, at higher calcination temperatures, the diffraction peak can be seen to become stronger, suggesting an increasing degree of graphitization. Furthermore, no diffraction peaks of Fe or Fe-based compounds can be observed for the samples prepared below 950 °C, consistent with results from TEM measurements which suggest atomic dispersion of the Fe species in the carbon matrix (Fig. 1), whereas two additional diffraction peaks emerge at $2\theta = 43.4^\circ$ and 44.5° for the FeNC-1050 sample, which can be ascribed to the (111) facet of Fe_3N (PDF#49-1622) and the (110) facet of face-centered cubic (*fcc*) iron (PDF#06-0696), respectively. That is, with a proper control of the pyrolysis temperature, the Fe species can be atomically doped into the carbon skeletons [41].

The degree of graphitization and defects of the samples were then investigated by Raman spectroscopy measurements. As shown in Fig. 2b, two broad and dominant peaks were observed at 1331 cm^{-1} and 1580 cm^{-1} for all FeNC samples, corresponding to the D and G peaks of graphitic carbon, again, suggesting successful carbonization of the MOF precursors [42]. Furthermore, one can see that the ratio of the D and G band intensity (I_D/I_G) decreases with increasing pyrolysis temperature, from 1.40 at 750 °C to 1.33 at 850 °C, 1.21 at 950 °C, and 1.17 at 1050 °C, suggesting an increasing degree of graphitization and hence electrical conductivity of the samples [43,44]. Nevertheless, the fact that $I_D/I_G > 1$ for all samples indicates the formation of a large number of defects in the materials, which may be beneficial to the adsorption and reduction of oxygen species.

The specific surface area and pore size distribution of the FeNC nanocomposites were then analyzed by nitrogen adsorption-desorption isotherm measurements. As shown in Fig. 3a, all samples exhibited combined characteristics of type I and IV isotherms, indicating the formation of both micropores and mesopores [45–48]. The adsorption curve in the high-pressure region had a clear upward trend, indicating that there were also secondary pores or macropores in the samples. This hierarchical porosity has been recognized to be beneficial for the diffusion of reactants and exposure of active sites. According to the multi-point BET equation, the specific surface area of FeNC was found to increase from 320.4 m^2 g^{-1} for FeNC-750 to 577.7 m^2 g^{-1} for FeNC-850, and 916.2 m^2 g^{-1} for FeNC-950, but then decreased to 863.0 m^2 g^{-1} for FeNC-1050 (Table 1). That is, the FeNC-950 sample exhibited the highest BET specific surface area among the series. Fig. 3b shows the pore size distributions of the samples, which entailed primarily micropores and mesopores, with the pore size mainly distributed from 0.6 nm to 40 nm, with FeNC-950 again exhibiting the largest pore volume of 1.51 m^3 g^{-1}, in comparison to 0.73 m^3 g^{-1} for FeNC-750, 0.96 m^3 g^{-1} for FeNC-850, and 1.30 m^3 g^{-1} for FeNC-1050.

XPS measurements were then carried out to examine the elemental composition and valence state of the FeNC composites. Fig. 4a shows the survey spectra of the series of samples, where the C, N, and O elements can be readily identified. For the FeNC-750 and FeNC-850 samples, Zn can still be seen; yet at pyrolysis temperatures higher than 950 °C, Zn species was effectively removed. The Fe element signals are relatively

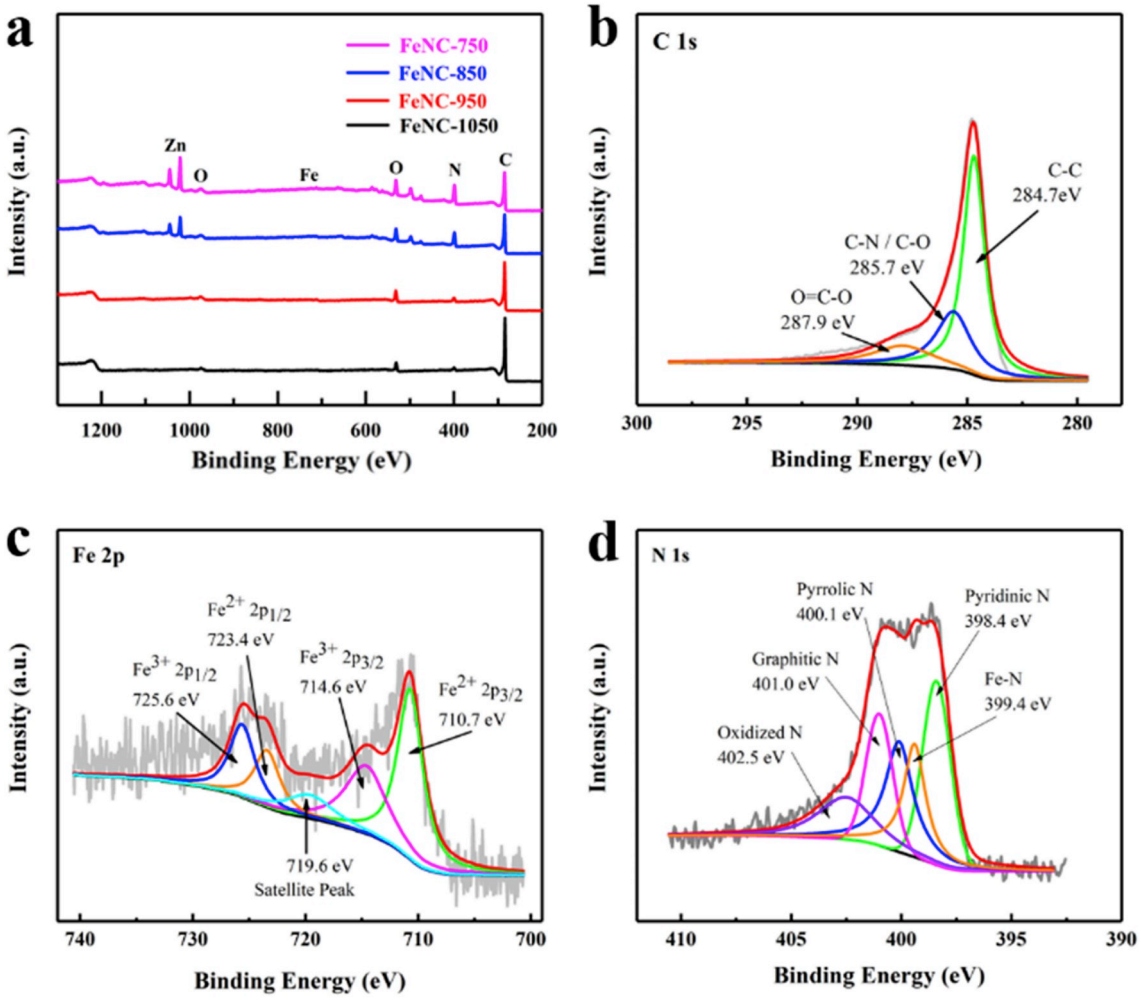

Fig. 4. (a) XPS survey spectra of the FeNC series. High resolution spectra of the (b) C 1s, (c) Fe 2p and (d) N 1s electrons of FeNC-950. Grey curves are experimental data and colored curves are deconvolution fits.

weak, suggesting low Fe contents (Table S1). Fig. 4b shows the high-resolution spectrum of the C 1s electrons in FeNC-950, which can be deconvoluted into three species, C═C (284.7 eV), C–O/C–N (285.7 eV), and O═C–O (287.9 eV) [49]. Fig. 4c shows the corresponding Fe 2p spectrum, where five subpeaks can be resolved at 710.7, 714.6, 719.6, 723.4 and 725.6 eV, corresponding to Fe^{2+} $2p_{3/2}$, Fe^{3+} $2p_{3/2,}$ satellite peaks, Fe^{2+} $2p_{1/2}$, and Fe^{3+} $2p_{1/2}$ respectively [50]. That is, only Fe^{2+} and Fe^{3+} species were produced in the FeNC-950 sample. The N 1s spectrum is shown in Fig. 4d (data for other samples are shown in Fig. S2), and five independent peaks can be resolved at 398.4, 399.4, 400.1, 401.0, 402.5 eV, corresponding to pyridinic, Fe–N, pyrrolic, graphitic, and oxidized nitrogen, respectively [11,51–55]. Notably, the FeNC-950 sample exhibited the highest content of Fe–N moieties among the FeNC series (Table S2), a unique feature that is considered to be responsible for ORR activity (*vide infra*) [56].

3.2. Electrochemistry

The ORR activities of the FeNC nanocomposites were then assessed and compared with commercial Pt/C (20 wt%) by RDE voltammetry in O_2-saturated 0.1 M KOH. The CV curves of all samples (Fig. 5a) showed a well-defined cathodic peak, suggesting apparent electrocatalytic activity towards ORR, as compared to the featureless profiles when the electrolyte solution was purged with N_2 [56]. Yet the activity varied among the series of FeNC samples. From the LSV data (Fig. 5b), one can see that the onset potentials (E_{onset}) increased from +0.82 V for FeNC-750 to +0.91 V for FeNC-850, and to +0.94 V for FeNC-950, but then decreased to +0.93 V for FeNC-1050. The corresponding half-wave potentials ($E_{1/2}$) and diffusion-limited currents changed in a similar trend, +0.73 V and 2.2 mA cm^{-2} for FeNC-750, +0.76 V and 4.17 mA cm^{-2} for FeNC-850, +0.84 V and 5.85 mA cm^{-2} for FeNC-950, and +0.81V and 5.52 mA cm^{-2} for FeNC-1050. For comparison, Pt/C exhibited an E_{onset} of +0.96 V and $E_{1/2}$ of +0.83 V. Taken together, these results show that FeNC-950 stood out as the best ORR catalyst among the series (Fig. 5c), with a performance on par with Pt/C and relevant catalysts reported in recent literature (Table S3). Note that Fe–N species have been found to play a critical role in the determination of the ORR activity [36,57], and results from XPS measurements (Tables S1 and S2) show that the FeNC-950 sample exhibits the highest Fe–N content among the series. In addition, in BET measurements, the FeNC-950 shows the highest specific surface area, which may facilitate the accessibility of the active sites. It is likely that these unique features collectively contribute to the remarkable ORR activity of FeNC-950, as compared to others.

The charge transfer kinetics of ORR was then analyzed by electrochemical impedance spectroscopy (EIS) measurements. Fig. 5d depicts the Nyquist plots acquired at open-circuit potential, which feature a semi-circle in the high frequency region and a straight line in the low-frequency region. One can see that the diameter of the semi-circle (charge-transfer resistance, R_{ct}) [58] varied among the series of samples, at 44.6 Ω for FeNC-750, 46.99 Ω for FeNC-850, 34.17 Ω for

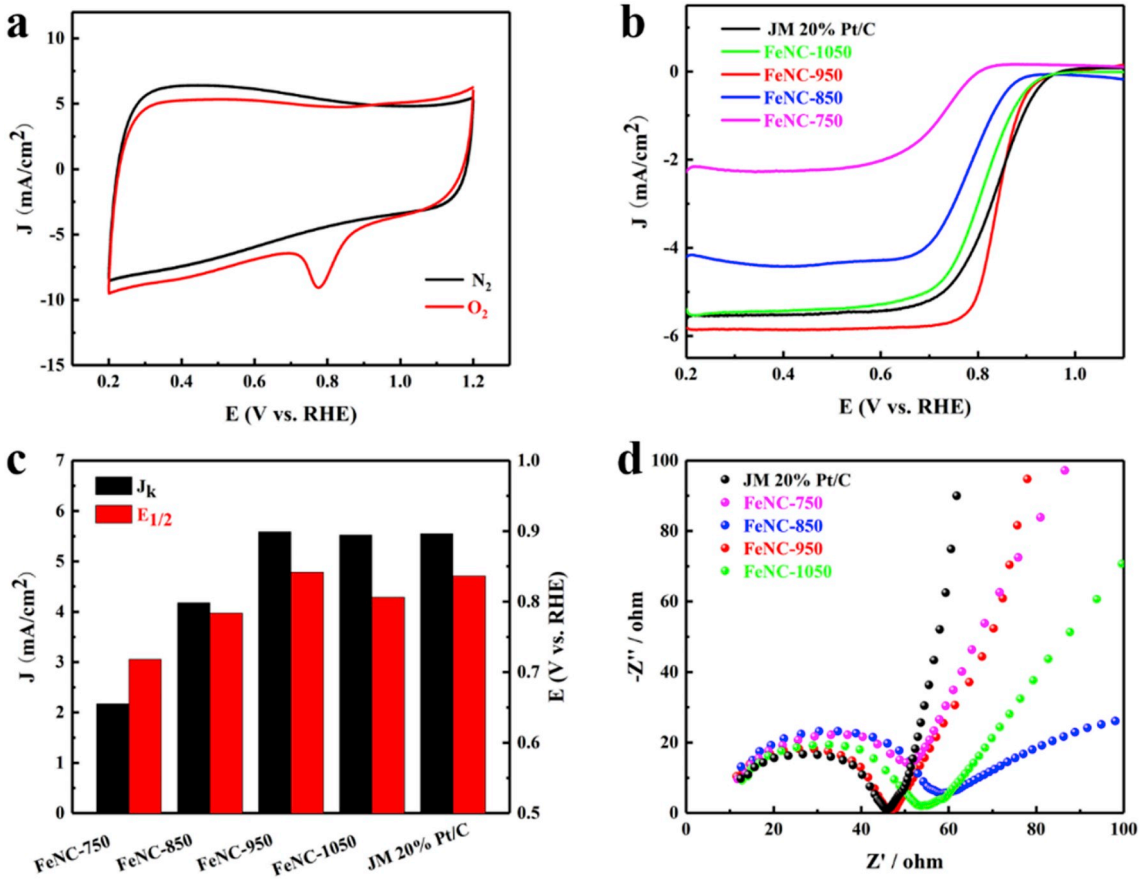

Fig. 5. (a) CV curves of FeNC-950 in N_2-saturated and O_2-saturated 0.1 M KOH solution at 50 mV s^{-1}. (b) LSV curves for different samples at the sweep rate 5 mV s^{-1} and rotation rate of 1600 rpm. (c) Comparison of J_k and $E_{1/2}$ for different catalysts. (d) EIS tests of the four FeNC catalysts and JM 20% Pt/C within the frequency range of 0.1 to 10^6 Hz at open-circuit potential.

FeNC-950, and 39.31 Ω for FeNC-1050, in comparison to 33.87 Ω for Pt/C. This is consistent with the observation that FeNC-950 exhibited the best ORR activity among the series.

To further investigate the ORR electron-transfer kinetics, RDE measurements were conducted at different rotation rates from 450 to 2500 rpm (Fig. 6a), and the Koutecky–Levich (K-L) plots (Fig. 6b) were used to analyze the kinetic parameters. As can be seen from Fig. 6a, the onset potential of FeNC-950 catalyst did not change with the increase of rotation rate. The good linearity of the corresponding K-L plots suggests first-order reaction kinetics toward the concentration of dissolved oxygen and similar electron transfer numbers (n) within the potential range of +0.80 to +0.90 V. In addition, it can be seen that as the rotation rate increased, the limiting current density increased accordingly [59]. Consistent results can be obtained in the number of electron transfer (n) and peroxide yield (H_2O_2%) at different potentials (Fig. 6c), where the average n value was 3.95 for FeNC-950, in comparison to 4.0 for Pt/C and the peroxide yield of FeNC-950 was below 5%. This indicates that oxygen reduction mostly followed the $4e^-$ pathway on FeNC-950 to water (OH^-). The Tafel slope of FeNC-950 (71.67 mV dec^{-1}) at low overpotentials was also slightly lower than that of Pt/C (77.1 mV dec^{-1}), indicating more efficient electron transfer on the FeNC-950 catalyst (Fig. 6d).

Accelerated durability tests were then carried out by cycling the catalyst over the potential range of +0.6 to +1.0 V at 50 mV s^{-1} in an O_2-saturated 0.1 M KOH solution. One can see that after 10,000 potential cycles, the $E_{1/2}$ of FeNC-950 showed only a negative shift of 11 mV (Fig. 7a), whereas the shift was much larger at 43 mV for Pt/C (Fig. 7b). In chronoamperometric measurements at +0.80 (Fig. 7c), one can see that 94.5% of its initial current density was retained with FeNC-950, while only 67.4% with Pt/C [60].

In addition to enhanced durability, FeNC-950 also exhibited excellent methanol tolerance. As depicted in Fig. 7d, one can see that the ORR activity decreased significantly for the Pt/C catalyst upon the addition of 3.0 M methanol, where the current actually became positive due to methanol oxidation, whereas no noticeable change was observed with FeNC-950 [61]. This result suggests that the FeNC-950 catalyst may serve as a promising cathode catalyst for direct methanol fuel cells.

4. Conclusion

In this study, by growing a bimetallic ZnFe-ZIF MOF onto polystyrene nanoparticle surface, Fe and N co-doped hollow carbon spheres were readily prepared by controlled pyrolysis of the obtained PS@ZnFe-ZIF core@shell precursors. Among the series, the sample prepared at 950 °C exhibited the best ORR performance in alkaline media with E_{onset} = +0.94 V and $E_{1/2}$ = +0.84 V, which was on par with leading results reported previously with relevant electrocatalysts and commercial 20 wt % Pt/C. Moreover, the FeNC-950 sample possessed superior long-term stability and better tolerance to methanol than the Pt/C catalyst. It is anticipated that this facile strategy can also be extended to other MOF-derived MNC hollow hybrids, thus opening up a new strategy for developing high-performance electrocatalysts for various energy-related applications.

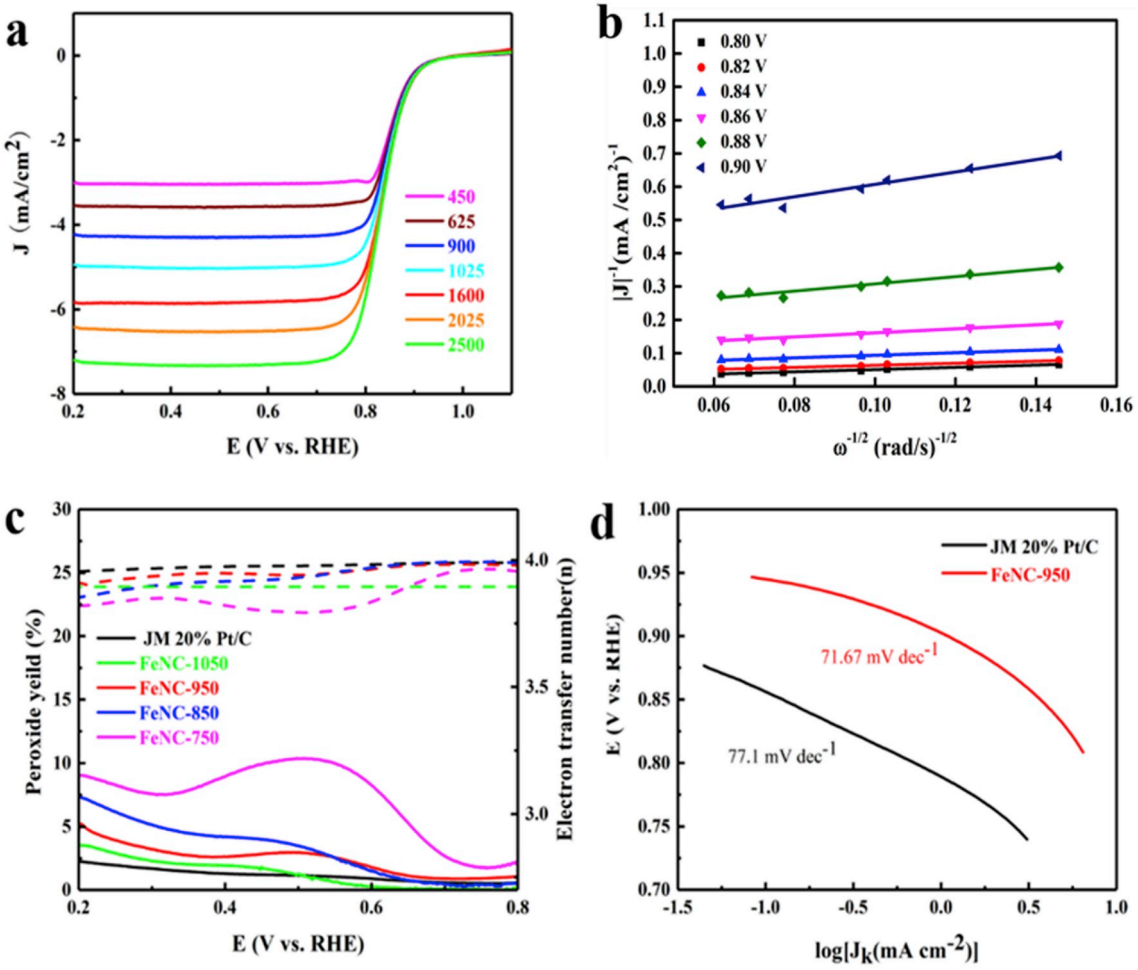

Fig. 6. (a) LSV curves at different rotation rates from 450 to 2500 rpm for FeNC-950. (b) K-L plots at different potentials from +0.80 to +0.90 V of FeNC-950. (c) Percentage of peroxide and the electron transfer number (n) curves calculated by RRDE. (d) Tafel plots of FeNC-950 (red) and JM 20% Pt/C (black) from RDE polarization curves. (For interpretation of the references to color in this figure legend, the reader is referred to the Web version of this article.)

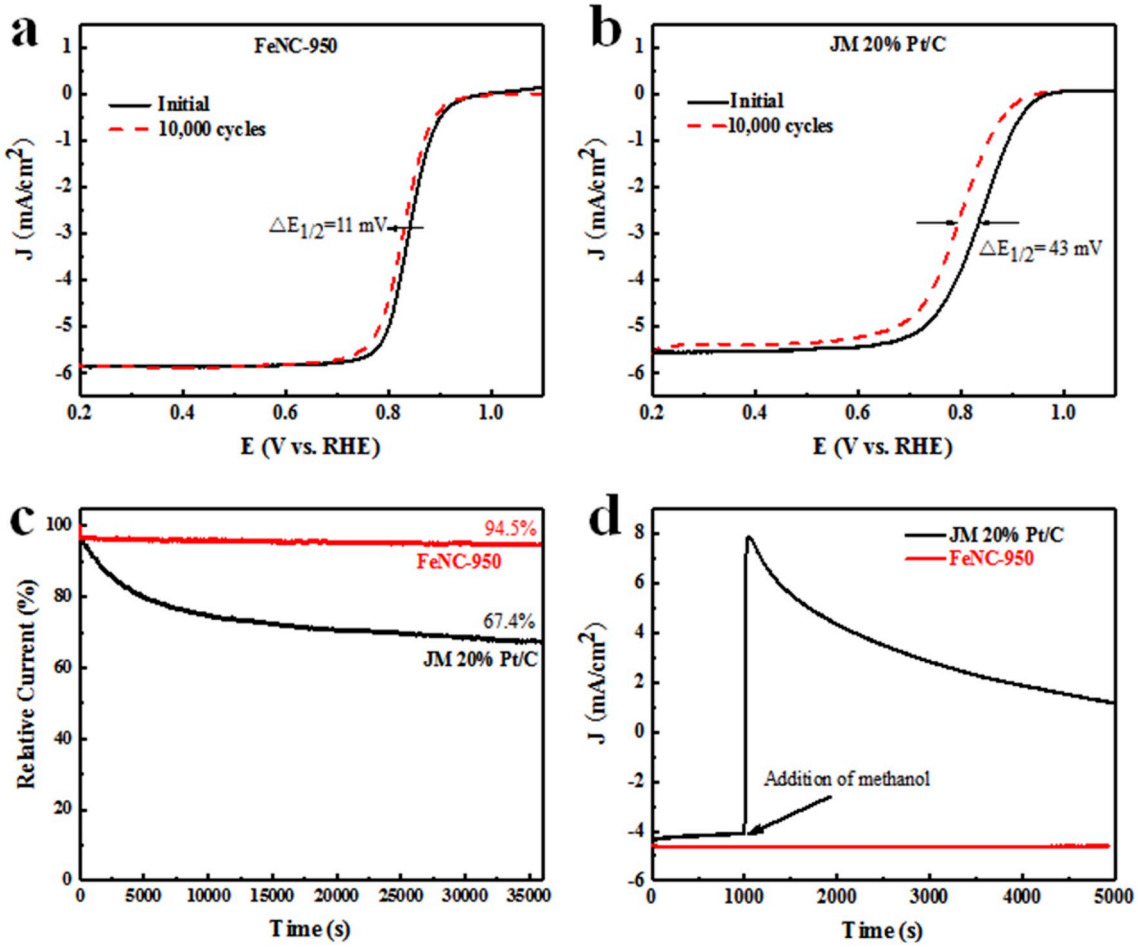

Fig. 7. LSV curves of (a) FeNC-950 and (b) JM 20% Pt/C before and after 10,000 potential cycles within +0.6 to +1.0 V (vs. RHE) in O_2-saturated 0.1 M KOH at the rotation speed of 1600 rpm. (c) Chronoamperometric curves of FeNC-950 and JM 20% Pt/C at +0.80 V (vs. RHE) in O_2-saturated 0.1 M KOH solution at a rotation rate of 1600 rpm. (d) Chronoamperometric curves of FeNC-950 and JM 20% Pt/C upon the addition of 3.0 M methanol at +0.80 V vs. RHE at the rotation rate of 1600 rpm.

Declaration of competing interest

The authors declare that they have no known competing financial interests or personal relationships that could have appeared to influence the work reported in this paper.

Acknowledgments

This study was supported by the National Natural Science Foundation of China (91745112), the Key Projects of Shanghai Committee of Science and Technology (15DZ1206902), and Science and Technology Commission of Shanghai Municipality (18020500800). S. W. C. thanks the National Science Foundation for partial support of the work (CHE-1710408 and CHE-1900235). Q. X. L. is supported by a research fellowship from the Shanghai Municipal Education Commission.

Appendix A. Supplementary data

Supplementary data to this article can be found online at https://doi.org/10.1016/j.jpowsour.2019.227659.

References

[1] W. Xia, A. Mahmood, Z. Liang, R. Zou, S. Guo, Angew. Chem. Int. Ed. 55 (2016) 2650–2676.
[2] M. Shao, Q. Chang, J.P. Dodelet, R. Chenitz, Chem. Soc. Rev. 116 (2016) 3594–3657.
[3] C.R. Raj, A. Samanta, S.H. Noh, S. Mondal, T. Okajima, T. Ohsaka, J. Mater. Chem. 4 (2016) 11156–11178.
[4] Y. Jiao, Y. Zheng, M. Jaroniec, S.Z. Qiao, Chem. Soc. Rev. 44 (2015) 2060–2086.
[5] C. Zhu, H. Li, S. Fu, D. Du, Y. Lin, Chem. Soc. Rev. 45 (2016) 517–531.
[6] S.-M. Jeong, M.K. Kim, G.-P. Kim, T.Y. Kim, S.-H. Baeck, Chem. Eng. J. 198–199 (2012) 435–439.
[7] Y. Xu, B. Zhang, Chem. Soc. Rev. 43 (2014) 2439–2450.
[8] B. You, P. Yin, L. An, Small 10 (2014) 4352–4361.
[9] C. Wang, N.M. Markovic, V.R. Stamenkovic, ACS Catal. 2 (2012) 891–898.
[10] J. Tymoczko, F. Calle-Vallejo, V. Colic, M.T. Koper, W. Schuhmann, A. S. Bandarenka, ACS Catal. 4 (2014) 3772–3778.
[11] H. Ren, Y. Wang, Y. Yang, X. Tang, Y.Q. Peng, H.Q. Peng, L. Xiao, J.T. Lu, H. D. Abruna, L. Zhuang, ACS Catal. 7 (2017) 6485–6492.
[12] H. Peng, F. Liu, X. Liu, S. Liao, C. You, X. Tian, H. Nan, F. Luo, H. Song, Z. Fu, P. Huang, ACS Catal. 4 (2014) 3797–3805.
[13] Y. Zhao, K. Watanabe, K. Hashimoto, J. Am. Chem. Soc. 134 (2012) 19528–19531.
[14] S. Kattel, G. Wang, J. Mater. Chem. 1 (2013) 10790–10797.
[15] T.S. Zhou, R.G. Ma, T. Zhang, Z.C. Li, M.H. Yang, Q. Liu, Y.F. Zhu, J.C. Wang, J. Colloid Interface Sci. 536 (2019) 42–52.
[16] J.S. Lee, G.S. Park, S.T. Kim, M. Liu, J. Cho, Angew. Chem. Int. Ed. 52 (2013) 1026–1030.
[17] S. Fu, C. Zhu, Y. Zhou, G. Yang, J.-W. Jeon, J. Lemmon, D. Du, S.K. Nune, Y. Lin, Electrochim. Acta 178 (2015) 287–293.
[18] J. Liang, R.F. Zhou, X.M. Chen, Y.H. Tang, S.Z. Qiao, Adv. Mater. 26 (2014) 6074–6079.
[19] X. Wan, H. Wang, H. Yu, F. Peng, J. Power Sources 346 (2017) 80–88.
[20] Y. Peng, B.Z. Lu, S.W. Chen, Adv. Mater. 30 (2018), 1801995.
[21] E. Proietti, F. Jaouen, M. Lefevre, N. Larouche, J. Tian, J. Herranz, J.P. Dodelet, Nat. Commun. 2 (2011) 416.
[22] D.F. Van Der Vliet, C. Wang, D. Tripkovic, D. Strmcnik, X.F. Zhang, M.K. Debe, R. T. Atanasoski, N.M. Markovic, V.R. Stamenkovic, Nat. Mater. 11 (2012) 1051.
[23] X. Wang, W. Zhong, Y. Li, Catal. Sci. Technol. 5 (2015) 1014–1020.
[24] S. Zhao, H. Yin, L. Du, L. He, K. Zhao, L. Chang, G. Yin, H. Zhao, S. Liu, Z. Tang, ACS Nano 8 (2014) 12660–12668.

[25] H. Yin, Z. Tang, Chem. Soc. Rev. 45 (2016) 4873–4891.
[26] Q. Lai, Y. Zhao, Y. Liang, J. He, J. Chen, Adv. Funct. Mater. 26 (2016) 8334–8344.
[27] X. Shen, H. Liu, X.B. Cheng, C. Yan, J.Q. Huang, Energy Storage Mater. 12 (2018) 161–175.
[28] B.Y. Xia, Y. Yan, N. Li, H.B. Wu, X.W.D. Lou, X. Wang, Nat. Mater. 1 (2016), 15006.
[29] T. Zhou, Y. Zhou, R. Ma, Z. Zhou, G. Liu, Q. Liu, Y. Zhu, J. Wang, Carbon 114 (2017) 177–186.
[30] F. Zhang, Y. Wei, X. Wu, H. Jiang, W. Wang, H. Li, J. Am. Chem. Soc. 136 (2014) 13963–13966.
[31] J. Long, K. Shen, L. Chen, Y. Li, J. Mater. Chem. 4 (2016) 10254–10262.
[32] K. Shen, X. Chen, J. Chen, Y. Li, ACS Catal. 6 (2016) 5887–5903.
[33] A. Aijaz, N. Fujiwara, Q. Xu, J. Am. Chem. Soc. 136 (2014) 6790–6793.
[34] F. He, G. Chen, Y. Zhou, Y. Yu, L. Li, S. Hao, B. Liu, J. Mater. Chem. 4 (2016) 3822–3827.
[35] H.X. Zhong, J. Wang, Y.W. Zhang, W.L. Xu, W. Xing, D. Xu, Y.F. Zhang, X.B. Zhang, Angew. Chem. Int. Ed. 53 (2014) 14235–14239.
[36] B.Z. Lu, T.J. Smart, D.D. Qin, J.E. Lu, N. Wang, L.M. Chen, Y. Peng, Y. Ping, S. W. Chen, Chem. Mater. 29 (2017) 5617–5628.
[37] R.G. Ma, G.X. Lin, Y. Zhou, Q. Liu, T. Zhang, G.C. Shan, M.H. Yang, J.C. Wang, npj Comp. Mater. 5 (2019) 1–15.
[38] Z. Cui, S. Wang, Y. Zhang, M. Cao, J. Power Sources 259 (2014) 138–144.
[39] P. Yin, T. Yao, Y. Wu, L. Zheng, Y. Lin, W. Liu, H. Ju, J. Zhu, X. Hong, Z. Deng, G. Zhou, S. Wei, Y. Li, Angew. Chem. Int. Ed. 55 (2016) 10800–10805.
[40] S. Liu, Z. Wang, S. Zhou, F. Yu, M. Yu, C.Y. Chiang, W. Zhou, J. Zhao, J. Qiu, Adv. Mater. 29 (2017), 1700874.
[41] Y. Qin, J. Yuan, L. Zhang, B. Zhao, Y. Liu, Y. Kong, J. Cao, F. Chu, Y. Tao, M. Liu, Small 12 (2016) 2549–2553.
[42] T. Zhou, R. Ma, T. Zhang, Z. Li, M. Yang, Q. Liu, Y. Zhu, J. Wang, J. Colloid Interface Sci. 536 (2019) 42–52.
[43] A. Zhu, P. Tan, L. Qiao, Y. Liu, Y. Ma, X. Xiong, J. Pan, Inorg. Chem. Front. 4 (2017) 1748–1756.
[44] Q.L. Zhu, W. Xia, T. Akita, R. Zou, Q. Xu, Adv. Mater. 28 (2016) 6391–6398.
[45] S.H. Joo, C. Pak, D.J. You, S.-A. Lee, H.I. Lee, J.M. Kim, H. Chang, D. Seung, Electrochim. Acta 52 (2006) 1618–1626.
[46] J. Yu, C.Y. Jimmy, M.K.-P. Leung, W. Ho, B. Cheng, X. Zhao, J. Zhao, J. Catal. 217 (2003) 69–78.
[47] K. Shen, W. Qian, N. Wang, C. Su, F. Wei, J. Mater. Chem. 2 (2014) 19797–19808.
[48] K. Shen, N. Wang, W. Qian, Y. Cui, F. Wei, Catal. Sci. Technol. 4 (2014) 3840–3844.
[49] H. Cheng, X. Feng, D. Wang, M. Xu, K. Pandiselvi, J. Wang, Z. Zou, T. Li, Electrochim. Acta 180 (2015) 564–573.
[50] Y. Zhao, K. Kamiya, K. Hashimoto, S. Nakanishi, J. Phys. Chem. C 119 (2015) 2583–2588.
[51] W. Martinezmillan, T. Toledanothompson, L. Arriaga, M. Smit, Int. J. Hydrogen Energy 34 (2009) 694–702.
[52] J. Zhang, Z. Zhao, Z. Xia, L. Dai, Nat. Nanotechnol. 10 (2015) 444–452.
[53] Y. Hu, J.O. Jensen, W. Zhang, Y. Huang, L.N. Cleemann, W. Xing, N.J. Bjerrum, Q. Li, ChemSusChem 7 (2014) 2099–2103.
[54] Y. Hu, J.O. Jensen, W. Zhang, S. Martin, R. Chenitz, C. Pan, W. Xing, N.J. Bjerrum, Q. Li, J. Mater. Chem. 3 (2015) 1752–1760.
[55] Y. Hou, T. Huang, Z. Wen, S. Mao, S. Cui, J. Chen, Adv. Energy Mater. 4 (2014) 1400337.
[56] C. Mao, A. Kong, Y. Wang, X. Bu, P. Feng, Nanoscale 7 (2015) 10817–10822.
[57] Z. Wang, Y. Lu, Y. Yan, T.Y.P. Larissa, X. Zhang, D. Wuu, H. Zhang, Y. Yang, X. Wang, Nano Energy 30 (2016) 368–378.
[58] X. Zhong, J. Chen, B. Liu, Y. Xu, Y. Kuang, J. Solid State Electrochem. 11 (2006) 463–468.
[59] S. Shanmugam, T. Osaka, Chem. Commun. 47 (2011) 4463–4465.
[60] A. Zadick, L. Dubau, N. Sergent, G. Berthomé, M. Chatenet, ACS Catal. 5 (2015) 4819–4824.
[61] N. Wu, Y. Wang, Y. Lei, B. Wang, C. Han, Y. Gou, Q. Shi, D. Fang, Sci. Rep. 5 (2015), 17396.